

Backscatter Coefficient Estimation Using Tapers with Gaps

Ultrasonic Imaging

1–18

© The Author(s) 2014

Reprints and permissions:

sagepub.com/journalsPermissions.nav

DOI: 10.1177/0161734614549263

ultrasonicimaging.sagepub.com



Adam C. Luchies¹ and Michael L. Oelze¹

Abstract

When using the backscatter coefficient (BSC) to estimate quantitative ultrasound parameters such as the effective scatterer diameter (ESD) and the effective acoustic concentration (EAC), it is necessary to assume that the interrogated medium contains diffuse scatterers. Structures that invalidate this assumption can affect the estimated BSC parameters in terms of increased bias and variance and decrease performance when classifying disease. In this work, a method was developed to mitigate the effects of echoes from structures that invalidate the assumption of diffuse scattering, while preserving as much signal as possible for obtaining diffuse scatterer property estimates. Backscattered signal sections that contained nondiffuse signals were identified and a windowing technique was used to provide BSC estimates for diffuse echoes only. Experiments from physical phantoms were used to evaluate the effectiveness of the proposed BSC estimation methods. Tradeoffs associated with effective mitigation of specular scatterers and bias and variance introduced into the estimates were quantified. Analysis of the results suggested that discrete prolate spheroidal (PR) tapers with gaps provided the best performance for minimizing BSC error. Specifically, the mean square error for BSC between measured and theoretical had an average value of approximately 1.0 and 0.2 when using a Hanning taper and PR taper respectively, with six gaps. The BSC error due to amplitude bias was smallest for PR ($N\omega = 1$) tapers. The BSC error due to shape bias was smallest for PR ($N\omega = 4$) tapers. These results suggest using different taper types for estimating ESD versus EAC.

Keywords

quantitative ultrasound, backscatter coefficient, tapers with gaps, specular echoes, spectral estimation

Introduction

The backscatter coefficient (BSC) is an important quantity that contains information about tissue microstructure. Quantitative ultrasound (QUS) parameters based on BSC estimates, such as the effective scatterer diameter (ESD) and effective acoustic concentration (EAC), have confirmed potential for improving medical diagnostics by classifying tissues.^{1–3} For example, studies have used QUS parameters to successfully examine ocular lesions,⁴ prostate,⁵ and liver⁶ tumors in rat

¹Department of Electrical and Computer Engineering, University of Illinois at Urbana–Champaign, Urbana, IL, USA

Corresponding Author:

Adam C. Luchies, Bioacoustics Research Lab, Department of Electrical and Computer Engineering, Beckman Institute, University of Illinois at Urbana–Champaign, 405 N Matthews Ave, Urbana, IL 61801, USA.

Email: luchies1@illinois.edu

models of breast cancer,⁷ and cancer in human lymph nodes.⁸ BSC estimation requires the assumption that incoherent scattering dominates the estimated backscattered signal power spectrum. This condition is satisfied when the interrogated medium is modeled using a single component that consists of echoes from diffuse scatterers (i.e., the medium contains a large number of randomly spaced nonresolvable scatterers per resolution cell).²

Biological tissues often contain complex structures that invalidate the assumed diffuse scatterer model necessary for BSC estimation techniques. These structures create nonstationarities in the backscattered signal that must be taken into account when parameterizing BSCs using diffuse scattering models. Previously, models have been proposed for the interrogated medium that include two^{9,10} or three^{11,12} scatterer components. The two-component models consist of diffuse (nonresolvable) scatterers and scatterers that produce resolvable echoes and have quasiperiodic spatial locations. The three-component models also include scatterers that produce resolvable echoes but that are nonperiodic (e.g., specular scatterers). After assuming a two- or three-component model, quantitative parameters (e.g., mean scatterer spacing) can be estimated and used to detect disease.^{9,10,12-14} In many of these studies, it was possible to estimate useful quantitative parameters without separating the signal components of the multicomponent models before analysis.

When estimating BSCs based from diffuse scattering (i.e., unresolvable scatterers), it is necessary to account for the coherent signal component (i.e., resolvable scatterers). The estimated backscattered signal power spectrum will include incoherent and coherent parts. When the medium is accurately modeled using a one-component model consisting of a collection of diffuse scatterers, the coherent part of the spectrum acts as noise compared with the incoherent part of the spectrum.¹⁵ In contrast, when a two- or three-component model is necessary to accurately model the medium (i.e., when resolvable echoes exist in the backscatter signal in nonrandom or random spatial arrangements), the incoherent part of the spectrum no longer dominates and the coherent part of the spectrum can significantly affect the shape of the estimated power spectrum and BSC.¹⁶ Furthermore, nondiffuse echoes also affect estimated QUS parameters by introducing bias and increasing variance of the estimated parameters.

In a previous study, we examined methods to identify data blocks with nondiffuse echoes, to estimate QUS parameters based on diffuse scatterers.¹⁶ The data blocks that contained nondiffuse echoes were removed entirely from the QUS parameter maps to create estimates based on diffuse scattering. Removal of the data blocks containing the nondiffuse scatterers from the QUS analysis increased clustering of the estimated QUS parameters among tissue collections, thereby improving the ability to uniquely classify tissues. Removal of an entire data block from the QUS analysis due to the presence of a nondiffuse echo also resulted in the exclusion of diffuse echo data. Frequently, the nondiffuse echoes filled only a small section of the data block, meaning some signals from diffuse echoes were not included in the analysis.

The goal of the present work is to develop a method to include the diffuse scattering echoes from data blocks containing nondiffuse echoes. The method involves generating tapers that have gaps (zero value) at the locations of nondiffuse echoes. Two classes of tapers with gaps were considered. The first class consisted of non-specially designed tapers (i.e., rectangular, Hanning, sinusoidal) forced to have zero value at the locations of nondiffuse echoes. Introducing a gap in this manner leads to undesirable signal truncation. The second class of tapers was specially designed and generated using an algorithm that considers the gap locations.¹⁷⁻¹⁹ These tapers gradually approach zero near the locations of the gaps and thus avoid the problems associated with signal truncation. The quality of BSC estimates was quantified in terms of bias and variance of estimates versus different tapers with gaps approaches. The method was validated using experimental backscattered signals from physical phantoms.

Method

BSC Estimation

Power spectral estimates for discretely sampled ultrasonic backscattered signals are usually calculated from a data block with axial (i.e., gate length) and lateral (i.e., number of scan lines) dimensions and that corresponds to a specific location in the tissue. The normalized backscattered signal power spectrum for a data block is defined here as^{2,3}

$$\bar{S}(k) = \frac{\gamma^2}{L} \sum_{l=0}^{L-1} \frac{S_l(k)}{S_{ref}(k)} \alpha(k), \quad (1)$$

where $S_l(k)$ is the windowed short-time Fourier transform of the l th scan line segment, $S_{ref}(k)$ is the windowed short-time Fourier transform of the backscattered signal from a planar reflector with reflection coefficient γ , $\alpha(k)$ is a function that compensates for attenuation, and L is the number of scan line segments included in the data block. A BSC estimate was made for each data block normalized power spectrum using a method described previously.^{20,21} QUS estimates can be obtained for each individual data block BSC, and a QUS map can be created by associating each data block with a pixel and assigning each pixel a color corresponding to the QUS estimate value.²²

RF Echo Model

Assuming multiple scattering and attenuation are negligible, the RF echo signal $y(t)$ is given as^{9,10}

$$y(t) = r(t) * h(t) = d(t) + c(t), \quad (2)$$

where $r(t)$ is the scatterer distribution function, $h(t)$ is the ultrasound impulse response, $d(t)$ is called the diffuse component and is the signal that results from the interaction of the ultrasound pulse with the diffuse scatterers, and $c(t)$ is the coherent component and is the signal that results from the interaction of the ultrasound pulse with the nondiffuse (i.e., resolvable) scatterers. The diffuse component is given as^{9,10}

$$d(t) = \sum_{n=1}^{N_d} s_{d,n}(t - \tau_n) * h(t), \quad (3)$$

where N_d is the number of diffuse scatterers, τ_n is the time delay for the n th diffuse scatterer, and $s_{d,n}(t)$ represents the scattering function for the n th diffuse scatterer. The coherent component is^{9,10}

$$c(t) = \sum_{m=1}^{N_c} s_{c,m}(t - \theta_m) * h(t), \quad (4)$$

where N_c is the number of scatterers in the coherent component, θ_m is the time delay for the m th coherent component scatterer, and $s_{c,m}(t)$ represents the scattering function of the m th coherent scatterer.

The power spectrum for the signal $y(t)$ is then given by

$$\begin{aligned} |Y(k)|^2 &= |H(k)R(k)|^2 = |H(k)|^2 |R(k)|^2 \\ &= |H(k)|^2 \left| \sum_{n=1}^{N_d} S_{d,n}(k) e^{-j2\pi k \tau_n} + \sum_{m=1}^{N_c} S_{c,m}(k) e^{-j2\pi k \theta_m} \right|^2, \end{aligned} \quad (5)$$

where $S_{d,n}(k)$ is the frequency domain representation of the scattering function for the n th diffuse scatterer and $S_{c,m}(k)$ is the frequency domain representation of the scattering function for the m th coherent scatterer. Considering a collection of uniform diffuse scatterers (i.e., $s_{d,n}(t) = s_d(t)$) and a single coherent scatterer (i.e., $N_c = 1$), the squared magnitude of the scatterer distribution function in Equation (5) is

$$\begin{aligned} |R(k)|^2 &= \left| S_d(k) \left(\sum_{n=1}^{N_d} e^{-j2\pi k \tau_n} \right) + S_c(k) e^{-j2\pi k \theta} \right|^2 \\ &= \left\{ \begin{aligned} &|S_d(k)|^2 \left(N_d + 2 \sum_{n \neq k}^{N_d} \cos(2\pi k (\tau_n - \tau_k)) \right) \\ &+ |S_c(k)|^2 + S_d(k) S_c^*(k) \sum_{n=1}^{N_d} e^{-j2\pi k (\tau_n - \theta)} \\ &+ S_c(k) S_d^*(k) \sum_{n=1}^{N_d} e^{j2\pi k (\tau_n - \theta)} \end{aligned} \right\}, \end{aligned} \quad (6)$$

where * indicates a complex conjugate. The coherent component scatterer term appears in three of the five summands. The shape of the spectrum will be a weighted sum incorporating the shape of the spectrum for the diffuse component signal and the shape of the spectrum for the coherent component signal. To estimate a spectrum that represents only the diffuse component signal, actions must be pursued to eliminate or reduce the effects of the coherent component signal. If the signal segments that include echoes from the coherent component scatterers can be identified, then it is possible to accomplish this task.

Signal Decomposition

Several methods have been proposed for decomposing the diffuse and coherent signal components. For example, multidirectional ultrasound has been used to separate directionally dependent specular reflections from diffuse scattering.²³ Because this method produces separate diffuse and coherent B-mode images and not RF data, the method is not useful for the current application. The WOLD decomposition was shown to be able to decompose diffuse and coherent signal components.²⁴ However, this method is restricted to situations when the coherent component contains periodic scatterers. The continuous wavelet transform (CWT) has also been proposed for signal decomposition.^{10,25} Compared with other time-frequency analysis methods, the CWT has superior frequency resolution (compared with the short-time Fourier transform) and does not suffer from cross product terms (compared with the Wigner–Ville distribution). For these reasons, the CWT signal decomposition method proposed in a previous study¹⁰ was selected for use in the current study.

The discrete realization of the CWT for a time-sampled sequence $y[n]$ with $n = 1, 2, \dots, N$ is defined as^{10,26}

$$W[s, n] = \sum_{n'=0}^{N-1} y[n'] \psi^* \left[\frac{(n' - n)}{s f_s} \right], \quad (7)$$

where s is the discrete wavelet scale value, f_s is the sampling frequency for the sequence, $\psi[n]$ is the sampled version of the selected mother wavelet $\psi_0[n]$ that has also been normalized.²⁷ The Morlet wavelet was selected for use in this study because this wavelet captures the general shape of the impulse response of an ultrasonic transducer. In addition, the results in a previous study¹⁰ indicated that the Morlet wavelet was more effective at detecting the coherent component

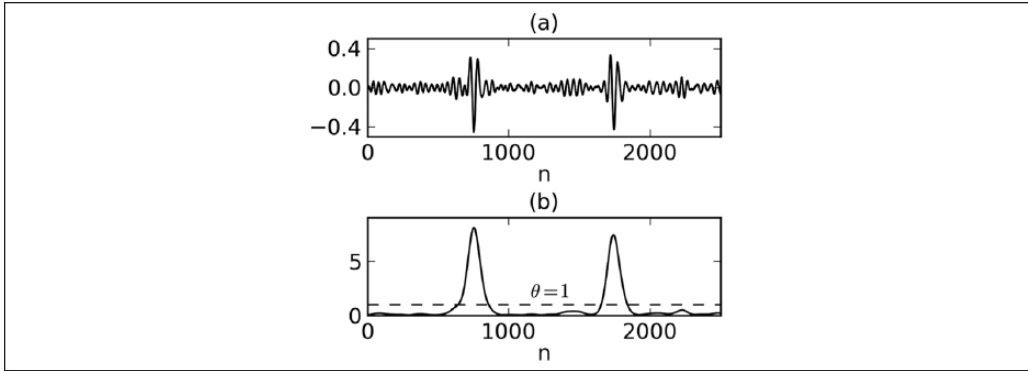


Figure 1. Example of (a) ultrasonic signal with specular echoes, (b) scale-averaged power (solid line) from the continuous wavelet transform, and threshold (dashed line) used to decompose diffuse and coherent components.

compared with the modulated cosine wavelet. The scales for the wavelet transform were selected using the process described in a previous study²⁷ to cover the entire frequency range content of the ultrasonic backscattered pulse.

The scale-averaged power (SAP) is defined as¹⁰

$$\overline{W}^2[n] = \frac{1}{J} \sum_{j=1}^J |W[s_j, n]|^2, \quad (8)$$

where s_j is the j th scale and a total of J scales are used. When an echo from a coherent component scatterer is present, a large fluctuation in the SAP at the time locations of the coherent component exists. To detect these fluctuations and separate the backscattered signal into diffuse and coherent components, the following decision rule can be used:¹⁰

$$\overline{W}^2[n] \underset{\text{coherent}}{\overset{\text{diffuse}}{\leq}} \mu_w + \theta \sigma_w, \quad (9)$$

where μ_w is the mean of the SAP, σ_w is the standard deviation of the SAP, and θ is a tunable parameter. An example of this thresholding process is shown in Figure 1. Several options exist for setting θ . For example, the data threshold could be displayed and a user might adjust θ as necessary. In addition, Monte Carlo simulations have been used previously to tune θ .¹⁰ The decision rule in Equation (9) allows for the creation of a binary mask that records whether each RF sample belongs to the diffuse or coherent component. After generating this mask, a windowing technique can be used to estimate the spectrum using only the RF samples that are included in the diffuse component.

Spectrum Estimation: Tapers with Gaps

Before BSC estimation, it is common to apply tapers such as the Hamming or Hanning tapers to the RF data. In this work, tapers with gaps were applied before estimating the BSC to remove coherent scattering signals from the calculation. A taper that is forced to have zero value at specific positions is said to contain a gap. The gap pattern vector \mathbf{I} , which is defined for $n = 1, 2, \dots, N$, where N is the length of the desired taper, is used to indicate the locations of gaps, such that $I[n] = 0$ at the locations of a gap and $I[n] = 1$ otherwise. A taper \mathbf{v} (also defined for $n = 1, 2, \dots, N$) can be forced to have gaps according to the gap pattern \mathbf{I} by performing the element-wise

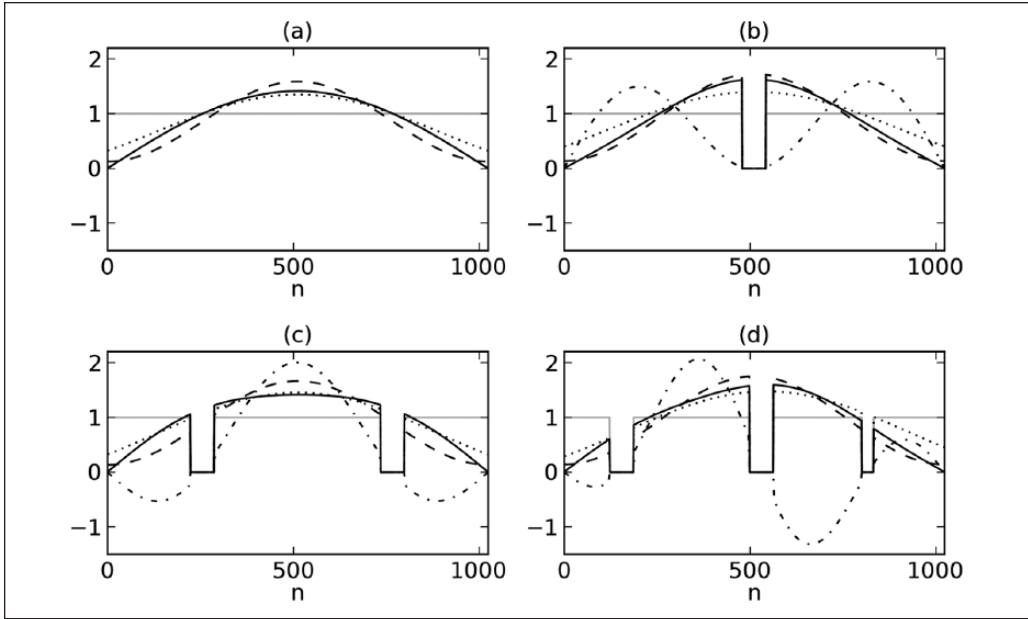


Figure 2. Examples of gap pattern (gray solid), Hanning taper (black solid), PR taper (dashed-dotted), MB taper (dashed), and SN tapers (dotted) with (a) no gap, (b) gap in the middle, (c) two gaps, and (d) three gaps. PR = prolate spheroidal; MB = minimum bias; SN = sinusoidal.

multiplication $v_i[n] = I[n]v[n]$. Examples of the Hanning taper with different gap patterns are illustrated in Figure 2. By applying tapers that have gaps at the times when the coherent component is present in the backscattered signal, tapered backscatter signals can be generated that only depend on the diffuse component, meaning BSC estimates based solely on the diffuse component can be calculated.

Several options exist for designing tapers with gaps. As previously mentioned, it is possible to project a gap pattern onto tapers such as the Hamming or Hanning tapers. There also exist families of tapers that minimize bounds on different measures of spectral bias, such as the discrete prolate spheroidal sequences (PR tapers)²⁸ and minimum bias tapers (MB tapers).²⁹

The rectangular taper with gaps (RG), which is also the gap pattern itself, was the first taper type examined in this work. The Hanning taper with gaps (HnG), a Hanning taper multiplied element-wise with the gap pattern, was also examined. The sinusoidal taper, generated according to

$$v^{(sn)}[n] = \sqrt{\frac{2}{N+1}} \sin\left[\frac{\pi n}{N+1}\right], \quad (10)$$

for $n = 1, 2, \dots, N$, was also examined. The sinusoidal taper with gaps (SNG) was generated using element-wise multiplication of the taper and the gap pattern. Examples of these different taper types are also illustrated in Figure 2.

Using element-wise multiplication to apply a gap pattern to rectangular, Hanning, or sinusoidal tapers causes the spectral shape of these tapers to change in uncontrollable ways, such as increased main lobe widths and side lobe levels that lead to increased bias and variance when estimating a spectrum. In contrast, discrete PR and minimum-bias tapers with gaps were designed specifically to offer control over spectral shape when generating these types of tapers, leading to reduced bias and variance when estimating a spectrum.

For a taper \mathbf{v} defined for $n = 1, 2, \dots, N$ and equal to zero otherwise, the energy in the frequency band $[-\omega, \omega]$ is given by

$$\eta^2(\omega) = \int_{-\omega}^{\omega} |V(f)|^2 df, \tag{11}$$

where $V(f)$ is the discrete-time Fourier transform of \mathbf{v} and $0 \leq \omega \leq 1/2$ is enforced due to the periodicity of $V(f)$. The PR taper is defined as the sequence that maximizes the fraction of energy in the band $[-\omega, \omega]$:²⁸

$$\mathbf{v}^{(pr)}[n] = \arg \max_{\mathbf{v}} \left\{ \frac{\eta^2(\omega)}{\eta^2(1/2)} \right\}, \tag{12}$$

where \mathbf{v} is selected from the set of sequences that have unit L_2 norm. When using the taper \mathbf{v} , the bias of the spectral estimate at frequency f_0 due to frequencies outside the range $[f_0 - \omega, f_0 + \omega]$ can be bounded in terms of $\eta^2(\omega)/\eta^2(1/2)$.²⁸ Therefore, the maximization in Equation (12) produces a taper that is optimal in the sense that it minimizes an upper bound on spectral bias. The solution to the maximization problem in Equation (12) is given by the eigenvector corresponding to the largest eigenvalue of the matrix given by¹⁷

$$A[n, m] = \int_{-\omega}^{\omega} e^{-j2\pi f(n-m)} df = \frac{\sin[2\pi\omega(m-n)]}{\pi(m-n)}, \tag{13}$$

for $m, n = 1, 2, \dots, N$. The process for converting the optimization problem in Equation (12) to the eigenvector analysis problem in Equation (13) can be found in a previous work.¹⁸ The PR taper with gaps corresponding to gap pattern vector \mathbf{I} is found by solving for the eigenvector corresponding to the largest eigenvalue of the matrix given by¹⁷

$$\begin{aligned} A_g[m, n] &= I[m]I[n]A[m, n] \\ &= I[m]I[n] \frac{\sin[2\pi\omega(m-n)]}{\pi(m-n)}. \end{aligned} \tag{14}$$

The gapped PR tapers were computed using the process described in a previous study.¹⁷ Examples of PR tapers with gaps are shown in Figure 2. For PR tapers, the bandwidth parameter used to design the tapers is often specified using the time-bandwidth product (TBP), $N\omega$ (where N is the total taper length and ω is the desired width of the main lobe of the frequency-domain representation of the taper). In this work, four PR taper types were generated having TBPs $N\omega = 1, 2, 3, 4$.

The MB taper of length N is defined as the sequence that minimizes the asymptotic expansion of the local bias $E[\hat{S}(f) - S(f)]$ and given by²⁹

$$\mathbf{v}^{(mb)}[n] = \arg \min_{\mathbf{v}} \left\{ \int_{-1/2}^{1/2} f^2 \left| \sum_{n=1}^N v[n] e^{-j2\pi fn} \right|^2 df \right\}, \tag{15}$$

where \mathbf{v} is selected from the set of sequences that have unit L_2 norm. The solution to the minimization problem in Equation (15) is given by the eigenvector corresponding to the largest eigenvalue of the matrix given by²⁹

$$\begin{aligned}
 B[m, n] &= \int_{-1/2}^{1/2} (1-f^2) e^{-j2\pi(m-n)f} df \\
 &= \begin{cases} \frac{11}{12}, & m = n \\ \frac{(-1)^{n-m+1}}{2\pi^2(n-m)^2}, & m \neq n \end{cases}, \quad (16)
 \end{aligned}$$

for $m, n = 1, 2, \dots, N$. The MB taper with gaps is the eigenvector corresponding to the largest eigenvalue for the matrix given by¹⁷

$$\begin{aligned}
 B_g[n, m] &= B[n, m]I[n]I[m] \\
 &= \begin{cases} \frac{11}{12}I[n]I[m], & n = m \\ \frac{(-1)^{n-m+1}}{2\pi^2(n-m)^2}I[n]I[m], & n \neq m \end{cases}. \quad (17)
 \end{aligned}$$

Examples of MB tapers with gaps are shown in Figure 2.

Experiments

The proposed methods for estimating BSCs using tapers with gaps were tested using data from a physical phantom. The physical phantom did not contain any scattering inclusions to cause signal segments to be sorted into the coherent signal component. In the first study, specular echoes were added artificially to the phantom data, detected using the CWT, and tapers with gaps were applied before estimating the BSC. In the second study, nonoverlapping segments having a length of one pulse length were randomly and successively added to the coherent component to create gap patterns. Gap patterns contained a specified number of gaps to evaluate the BSC estimation performance as a function of the total number of gaps. The goal of the study was not to detect coherent components, as this was established in a previous study.¹⁶ The goal of this study was to evaluate how the different tapers with gaps affected estimates of the BSC. Tapers with gaps were designed for these random configurations, BSCs were estimated using the designed tapers and compared with the theoretical BSC for the phantom. In the third study, a physical phantom containing wire targets to provide true specular echoes was studied and used to evaluate the proposed methods.

Physical Phantom Data Collection

To evaluate the tapering with gaps method, BSC estimates were obtained from measurements from an agar phantom with glass bead inclusions. The phantom contained 47 glass spheres/mm³ ranging in diameter from 36 to 48 μm . Ultrasound was transmitted into the phantom through a layer of thin plastic film. The transmission coefficient through the film was compensated using the method described in a previous study.³⁰ The phantom was scanned using a 1.27-cm diameter single-element transducer ($f/4$) having a nominal 10-MHz center frequency and -10 -dB bandwidth of 13 MHz. The phantom was raster scanned in one plane over a 4 cm by 1 cm area. A reference spectrum $S_{ref}(f)$ was obtained from a planar Plexiglas reflector ($\gamma \approx 0.37$). Data blocks

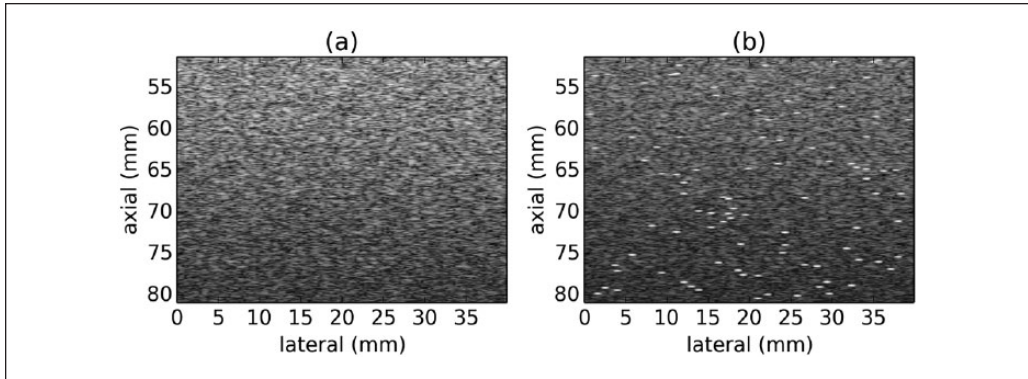


Figure 3. Example B-mode images of phantom data (a) without and (b) with specular echoes.

were square with sides equal to 30 wavelengths of the transducer center frequency. Data block overlapping was 75% with the purpose of smoothing the average BSC estimate.

Random Specular Echoes

Specular echoes were artificially added to the phantom data to test tapers with gaps. The specular echo was designed using the reflected waveform from a planar reflector placed at the focus of the transducer. This waveform was convolved with a spherical Gaussian scatterer model having ESD of 100 μm . The specular echoes were given amplitude values of approximately 10 dB relative to the amplitude of the diffuse scatterers in the phantom. Specular echoes were positioned according to a Poisson distribution and four specular echo concentrations were examined, including 0.25, 0.50, 0.75, and 1.0 echoes/ mm^3 . Examples of the phantom data with and without specular echoes are shown in Figure 3. The CWT was used to create a binary mask indicating diffuse and specular scattering regions. Tapers with gaps were generated for the considered family of tapers. The BSC was estimated for each data block using the tapers with gaps for that particular data block. These BSCs were averaged together to form a representative BSC for the phantom, which was compared with the BSC estimated when no specular echoes were added to the phantom data.

Gap Pattern Progressions

An example of a single gap pattern progression containing gap patterns with zero, one, two, and three gaps is illustrated in Figure 4. Gap pattern progressions were generated according to the following procedure: the first gap pattern in the progression contained no gaps, the second gap pattern in the progression contained a single gap at a random location, and the n th gap pattern in the progression contained the gaps from the previous gap patterns in the progression, in addition to a new gap at a random location. All gaps were one pulse length and nonoverlapping. For each gap pattern in the progression (i.e., zero gaps, one gap, two gaps, etc.), all taper types were generated. BSC estimates were calculated using each of the taper types separately; that is, rectangular, Hanning, SN, MB, PR ($N\omega = 1$), PR ($N\omega = 2$), PR ($N\omega = 3$), and PR ($N\omega = 4$) for all gap patterns in the gap progression. The process produced a BSC progression for each taper type, allowing for the evaluation of the effect that a taper had on the BSC as gaps were successively added to the gap pattern. A total of 10 gap pattern progressions were generated. Each gap pattern progression contained 10 gap patterns, the first gap pattern had zero gaps, the second had one gap, the third

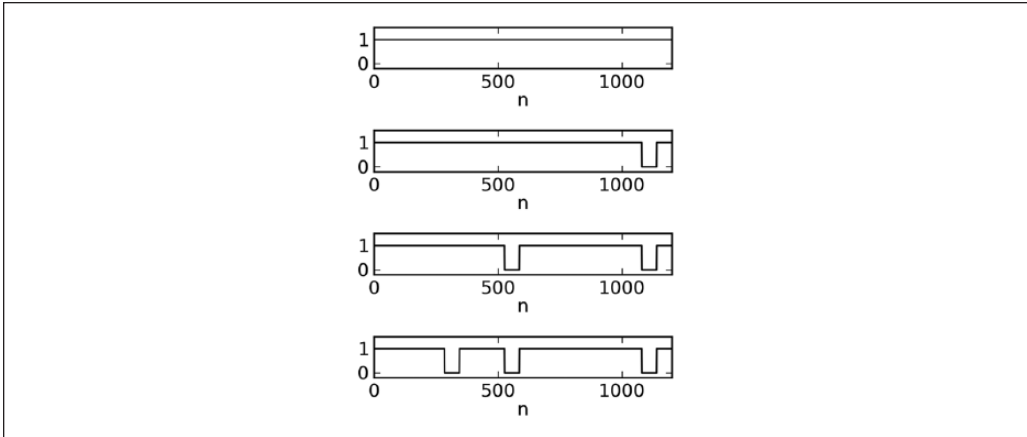


Figure 4. Example of a single gap pattern progression containing gap patterns with zero, one, two, and three gaps. Gaps are randomly located and nonoverlapping.

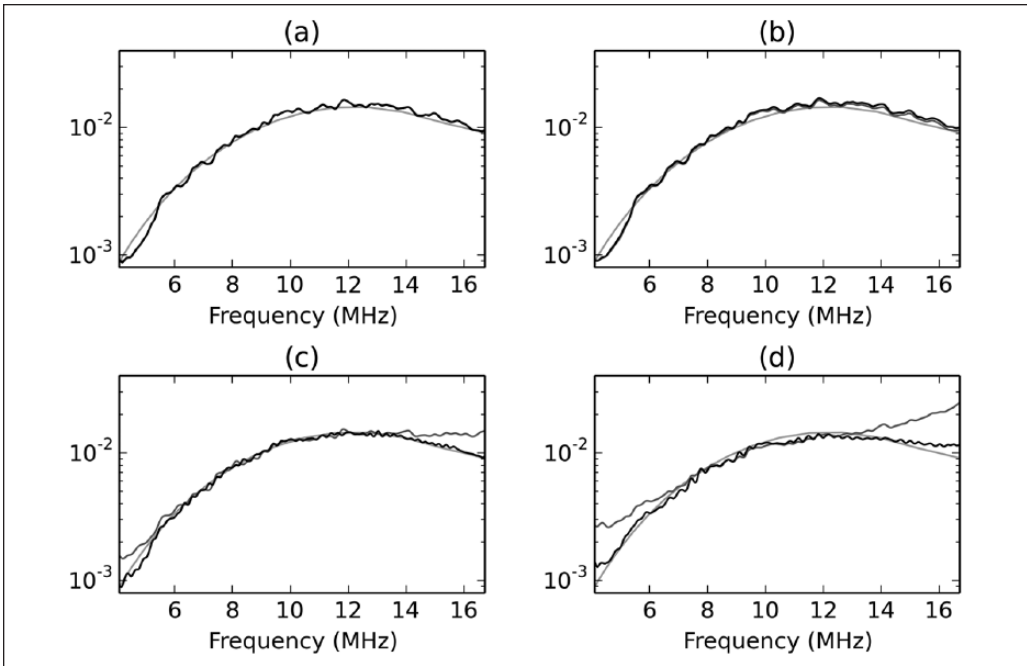


Figure 5. Example of BSC theory (light gray) with BSC estimates using an MB taper with gaps (black) and a Hanning taper with gaps (dark gray) for (a) one gap, (b) two gaps, (c) four gaps, and (d) six gaps (individual gaps are one pulse length). BSC = backscatter coefficient; MB = minimum bias.

had two gaps, and so forth, with the last having nine gaps. The 10 gap patterns were used to generate 10 BSC progressions for each taper type. Examples of BSC estimates for a physical phantom are shown in Figure 5 for several gap patterns from a single gap pattern progression and two different taper types. From Figure 5, it can be observed that the spectrum changes shape as the number of gaps increases.

Wire Target Phantom

BSC estimates were obtained from measurements of an agar-graphite phantom with four tungsten wire targets having a diameter of 100 μm included to produce specular echoes. Graphite was included in the phantom to provide scattering and to achieve an attenuation coefficient slope value of 0.5 dB/cm-MHz. The wire targets were placed parallel to each other. First, the phantom was scanned in the plane perpendicular to the wire targets to provide data blocks containing specular echoes. Second, the phantom was scanned parallel to and away from the wire targets to provide data blocks without specular echoes. The protocol for scanning the physical phantom was described above and was repeated for this phantom. The CWT was used to create a binary mask indicating diffuse and specular scattering regions. Tapers with gaps were generated for the considered family of tapers. The BSC was estimated for each data block using the tapers with gaps for that particular data block. These BSCs were averaged together to form a representative BSC for the phantom, which was compared with the BSC estimated when no specular echoes were present in the phantom data.

Performance Assessment

To quantitatively assess the performance of the different types of tapers examined, the fit between the estimated and theoretical BSCs was quantified using three different error metrics.

The first metric studied was the mean square error (*MSE*) defined by

$$MSE = \frac{1}{N} \sum_{i=1}^N \left[X(\eta(k_i), \eta_0(k_i)) \right]^2, \quad (18)$$

where $\eta(k)$ is the BSC estimated using tapers with gaps and $\eta_0(k)$ is the theoretical BSC. The log difference between two BSC functions $\eta_1(k)$ and $\eta_0(k)$ is given by

$$X(k_i) = 10 \log_{10}(\eta(k_i) / \eta_0(k_i)), \quad (19)$$

where k represents the spatial sampling frequency and i represents the index for the discretely sampled BSC data. The *MSE* is a general error metric that incorporates errors due to both amplitude (bias) and frequency-dependent (shape) errors. To distinguish between these two effects, two other error metrics were considered given by²¹

$$E_a = \frac{1}{N} \sum_{i=1}^N X(\eta(k_i), \eta_0(k_i)),$$

$$E_f = \sqrt{\frac{1}{N} \sum_{i=1}^N \left[X(\eta(k_i), \eta_0(k_i)) - E_a \right]^2}, \quad (20)$$

where E_a measures the amplitude agreement and E_f measures the frequency-dependent agreement between the estimated and theoretical BSCs. The E_a metric quantifies EAC estimate error and the E_f metric quantifies ESD estimate error.

Results

Random Specular Echoes

After adding specular echoes in varying concentrations to the phantom data, the *MSE*, E_a , and E_f error metrics for the BSC estimated with and without specular echoes were calculated. After identifying the diffuse and coherent components using the CWT, the different tapers with gaps

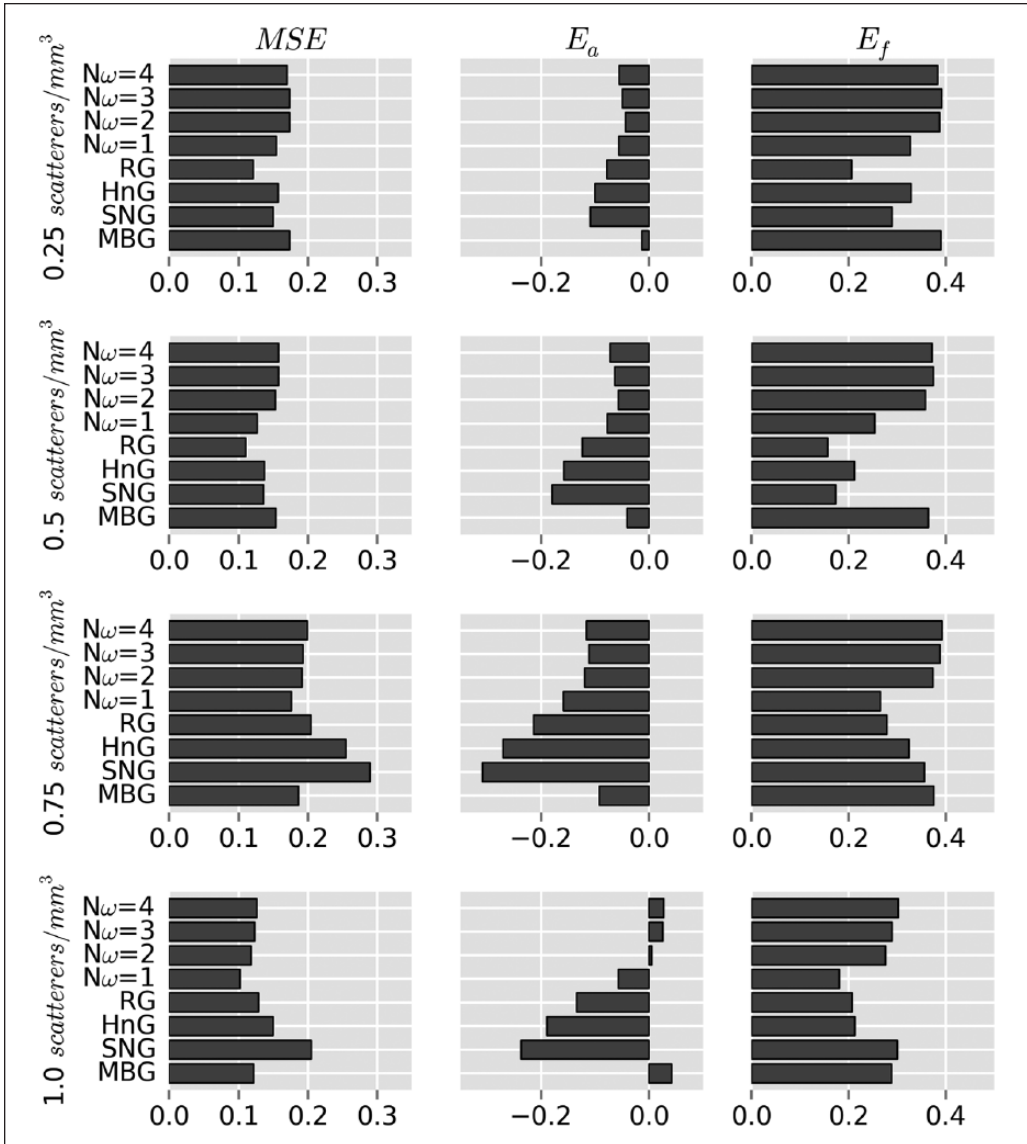


Figure 6. BSC error metrics, including MSE (left column), E_a (middle column), and E_f (right column) for different concentrations of specular echoes. Results are displayed for all taper types. BSC = backscatter coefficient; MSE = mean square error; RG = rectangular taper with gaps; HnG = Hanning taper with gaps; SNG = sinusoidal taper with gaps; MBG = minimum-bias tapers with gaps.

families were applied to the data, and a BSC was estimated for each taper family. The resulting error metric magnitudes were at least an order of magnitude less when using any of the taper with gaps family compared with using tapers without gaps. Therefore, the comparison only considers the error metrics among the different families of tapers with gaps to determine the family best able to reduce the BSC error introduced by the specular echoes.

The MSE , E_a , and E_f error metrics were calculated from the BSCs for each taper with gaps family and for each concentration of specular echoes and the results are shown in Figure 6. From Figure 6, the MSE and E_f error metrics take their lowest values when using RG tapers for lower

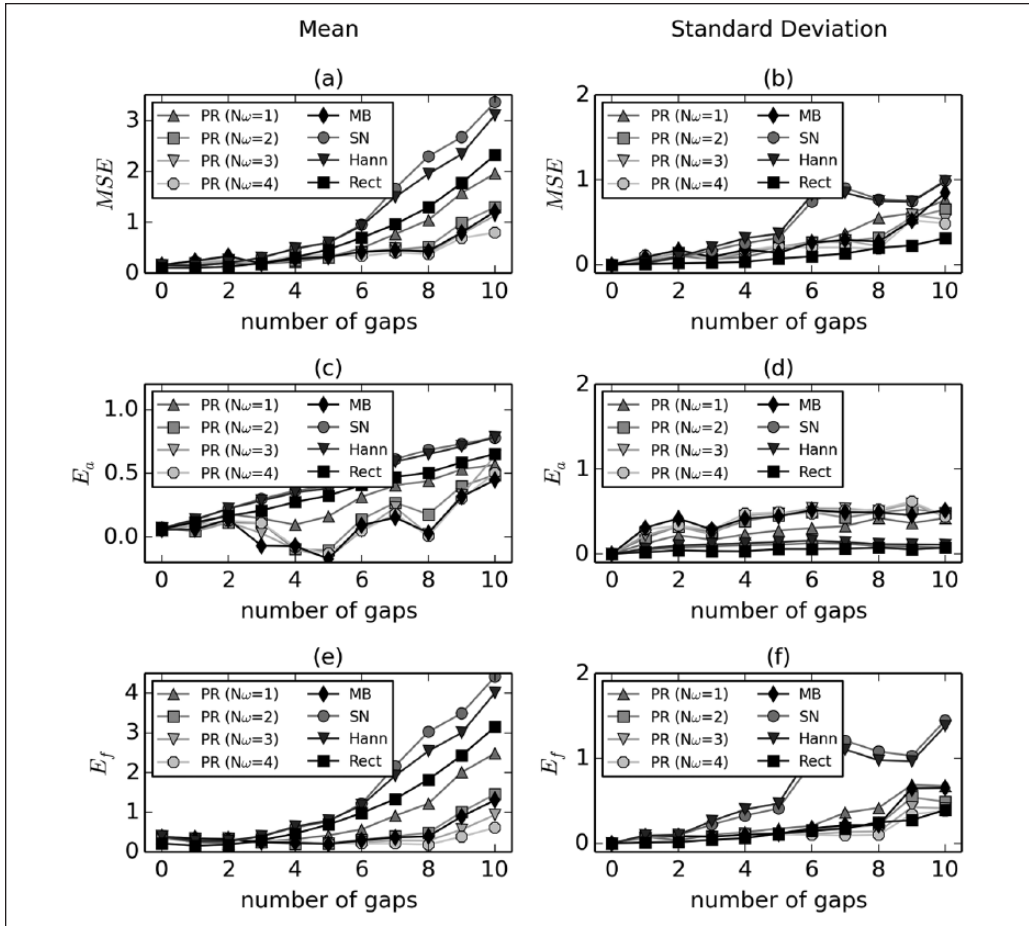


Figure 7. Three BSC error metrics, including (a, b) MSE , (c, d) E_a , and (e, f) E_f . Mean (left) and standard deviation (right) values for 10 gap pattern progressions displayed as a function of the number of gaps in the gap pattern. Mean and standard deviation values have the same units as the error metrics that they represent. BSC = backscatter coefficient; MSE = mean square error; PR = prolate spheroidal; MB = minimum bias; SN = sinusoidal.

concentrations of specular echoes (i.e., 0.25 and 0.50 scatters/mm³). For these same concentrations, the E_a error metric is lowest for the MB tapers. For the higher concentrations of specular echoes (i.e., 0.75 and 1.0 scatters/mm³), the PR taper with $N\omega = 1$ gives the lowest values for the MSE and E_f error metrics. For these higher specular echo concentrations, the PR tapers also give lower values for the E_a error metric when compared with the non-specially designed tapers.

Gap Pattern Progressions

The MSE , E_a , and E_f error metrics were found using the BSCs for each taper type and for each gap pattern of each gap pattern progression. For a single taper type, the mean of a selected error metric was computed as a function of the number of gaps in the gap pattern (i.e., the mean value was found when using zero gaps, another mean value found when using one gap, etc.). The mean value for the MSE , E_a , and E_f error metrics displayed as a function of the number of gaps in the gap pattern is shown in Figure 7. The purpose of the analysis is to determine the effect that the

number of gaps in a gap pattern has on BSC error for a selected taper type. From Figure 7(a), the mean MSE was approximately the same for all the types of tapers examined in the range of zero to five gaps, indicating that there is little to no advantage to using MB or PR tapers compared to the other types of tapers. In the range of 6 to 10 tapers, the Hanning and sinusoidal tapers provided the worst performance, followed by the rectangular and PR ($N\omega = 1$) tapers. The PR ($N\omega = 2$, $N\omega = 3$, $N\omega = 4$) tapers and the MB tapers produced BSC estimates with the smallest MSE error metric values.

From Figure 7(c), the mean E_a metric was approximately the same for all tapers in the range of zero to two gaps. In the range of 3 to 10 gaps, the Hanning and sinusoidal tapers provided the worst performance, followed by the rectangular and PR ($N\omega = 1$) tapers. The PR ($N\omega = 2$, $N\omega = 3$, $N\omega = 4$) tapers and the MB tapers offered the best performance for the E_a metric in this range.

From Figure 7(e), the mean E_f metric was approximately the same for all tapers in the range of zero to three gaps. In the range of 4 to 10 gaps, the Hanning and sinusoidal tapers provided the worst performance, followed by the rectangular tapers, followed by the PR ($N\omega = 1$), followed by the MB and PR ($N\omega = 2$) tapers. The PR ($N\omega = 3$, $N\omega = 4$) tapers offered the best performance for the E_f metric in this range.

From Figure 7(b), (d), and (f), the large standard deviation values indicate that the number of gaps in a taper is a poor indicator for assessing the effect that a taper with gaps has on a BSC estimate and a different taper descriptor is needed.

The spectral concentration (SC) of a taper is given by the amount of energy in the main lobe of the frequency representation for the taper. If the main lobe for the taper is in the frequency band $[-\omega_{ML}, \omega_{ML}]$, then using Equation (13), the SC is defined as

$$SC = \frac{\eta^2(\omega_{ML})}{\eta^2(1/2)}. \quad (21)$$

The SC value serves as a quality metric for a taper. SC values close to 1.0 indicate that the side lobe levels for the taper are low compared with the main lobe. SC s much less than 1.0 indicate that the side lobe levels are at the same level or just below the main lobe. If a taper has an SC much less than 1.0, spectral bias can significantly affect the shape of the estimated BSC, as shown in Figure 5. Therefore, the SC for a taper can provide some insight when predicting whether a taper will produce a biased BSC estimate or not. The MSE , E_a , and E_f error metrics are displayed as a function of taper SC in Figure 8. Based on the analysis of Figure 7, the results are only presented for PR ($N\omega = 1$, $N\omega = 2$, $N\omega = 3$, $N\omega = 4$) tapers. From Figure 8, the PR ($N\omega = 1$) taper type has the widest range of SC s. In fact, the range of SC values decrease for the higher values of $N\omega$ and is smallest for the PR ($N\omega = 4$) taper. The result is not surprising because the PR ($N\omega = 1$) taper has the narrowest main lobe width, making it more difficult to fill the main lobe with energy, compared with the PR ($N\omega = 4$) taper type with the widest main lobe width.

From Figure 8(a) to (d), the MSE error metric increased as SC decreased for all taper types. The PR ($N\omega = 1$) taper produced the largest MSE values, whereas the PR ($N\omega = 4$) produced the smallest. However, the PR ($N\omega = 1$) taper produced the best curve for predicting MSE based on SC . For example, in the SC range 0.75 to 1.0 for the PR ($N\omega = 1$) taper, the MSE values were in the range 0 to 0.2. In contrast, for the PR ($N\omega = 4$) taper in the SC range 0.75 to 1.0, the MSE values ranged from 0 to 1.1 (several tapers with SC s close to 1.0 had MSE s greater than 1.0). Therefore, for the PR ($N\omega = 4$) taper, SC serves as a poor indicator for MSE compared with using the PR ($N\omega = 1$) taper.

From Figure 8(e) to (h), the range of E_a values increased as SC decreased for all taper types. The PR ($N\omega = 1$) taper produced the lowest range of E_a values. Similar to the MSE metric, the PR ($N\omega = 1$) taper produced the best curve for predicting E_a based on SC . For example, in the

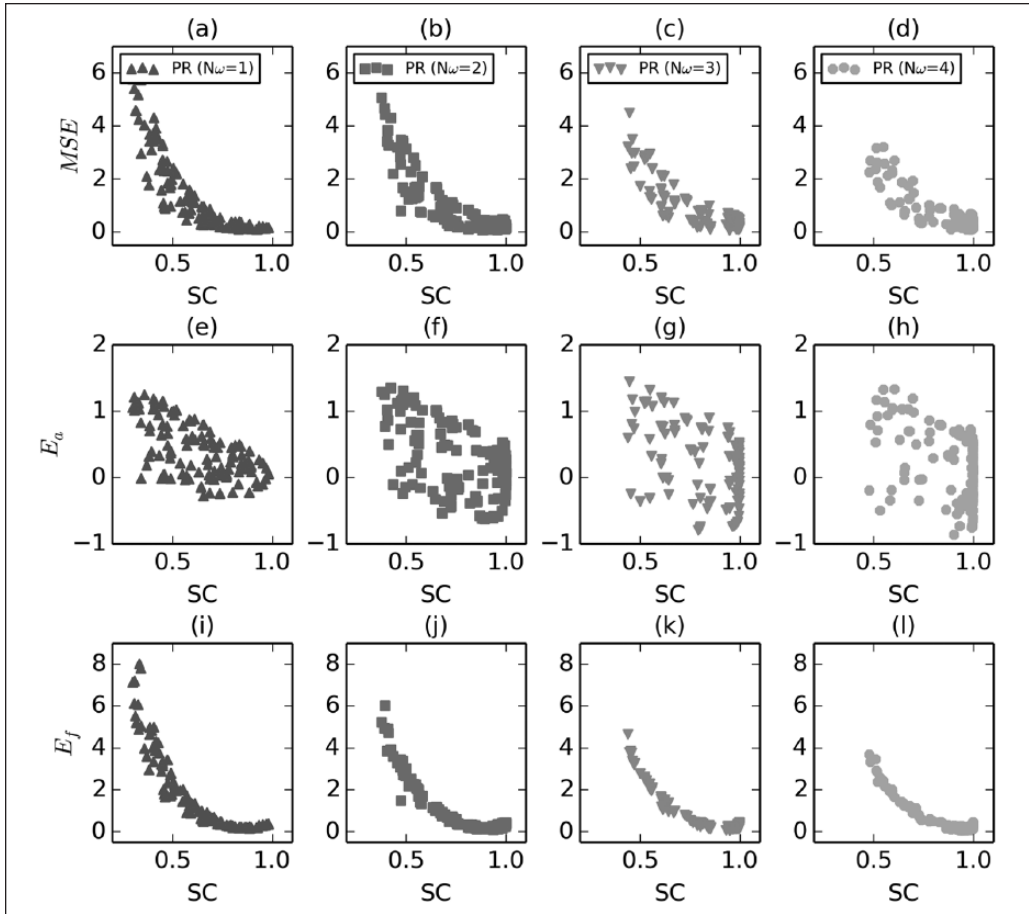


Figure 8. Three BSC error metrics, including MSE , E_a , and E_f displayed as a function of SC for PR ($N_\omega = 1$, $N_\omega = 2$, $N_\omega = 3$, $N_\omega = 4$) taper types. BSC = backscatter coefficient; MSE = mean square error; SC = spectral concentration; PR = prolate spheroidal.

SC range 0.75 to 1.0 for the PR ($N_\omega = 1$) taper, the E_a values were in the range -0.2 to 0.5 . In contrast, for the PR ($N_\omega = 4$) taper in the SC range -0.9 to 1.0 , the E_a values ranged from -0.75 to 1.0 (tapers having an SC close to 1.0 had E_a values in the range of -0.9 to 0.8). Therefore, for the PR ($N_\omega = 4$) taper, SC serves as a poor indicator for E_a compared with using the PR ($N_\omega = 1$) taper.

From Figure 8(i) to (l), the E_f error metric increased as SC decreased for all taper types. The PR ($N_\omega = 4$) taper produced the lowest E_f values. In addition, all taper types produced similar curves for predicting E_f values based on SC .

Wire Target Phantom

The MSE , E_a , and E_f error metrics were found using the BSCs for each taper type and the results are shown in Figure 9. From Figure 9, all of the error metrics are minimal for the PR ($N_\omega = 4$). The next best tapers are the PR ($N_\omega = 3$) and HnG tapers. The MB and RG tapers had the largest errors.

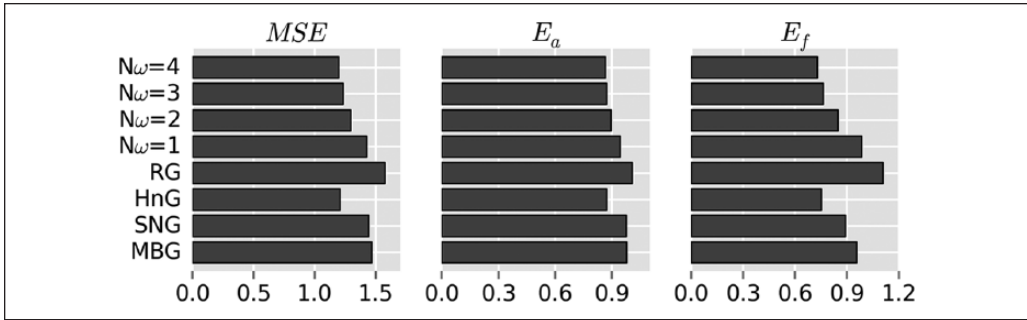


Figure 9. Three BSC error metrics, including MSE , E_a , and E_f for the wire target phantom. BSC = backscatter coefficient; MSE = mean square error; RG = rectangular taper with gaps; HnG = Hanning taper with gaps; SNG = sinusoidal taper with gaps; MBG = minimum-bias tapers with gaps.

Discussion

The results of Figure 6 suggest that PR tapers offer an advantage over non-specially designed tapers for the higher concentrations of specular echoes. For lower concentrations of specular echoes, the non-specially designed rectangular taper with gaps offered the best performance for two out of the three error metrics.

The results of Figure 7 suggest that the PR tapers are the best choice of taper type for the tapers with gaps method. These taper types, on average, produced the lowest values for the three examined BSC error metrics.

The results of Figure 8 provide further insight into how to utilize the PR tapers in the tapers with gaps method. The SC parameter might be used to determine if a BSC estimate from a generated PR taper can be trusted or not. For example, one of the BSC error metrics might be selected along with a cutoff value. BSC estimates with error metric values above the cutoff are deemed unacceptable. The BSC error metric cutoff can then be matched to a SC value using scatter plots similar to those shown in Figure 8. If a generated taper has an SC below a cutoff value, that particular scan line is deemed to be unreliable and is excluded from the BSC average for the data block.

The three selected error metrics provide different information about the effect that the taper with gaps might have on a BSC estimate. The MSE error provides an overall error effect. The E_a provides information about the bias (vertical shift) effect that the taper might produce. The E_f provides information about the frequency-dependent (shape) effect that the taper might produce. Based on the particular application one error metric might make more sense to use than the others. For example, if estimating ESD from BSC estimates, the E_f error metric should be selected because the ESD depends on the BSC shape. If estimating the EAC from BSC estimates, the E_a error metric should be selected because the EAC depends more on the amplitude of the BSC than the shape. If not using the BSC to estimate other QUS parameters, then MSE error metric is the best choice.

Once the appropriate error metric has been selected, the taper type can be selected. If using the MSE error metric, the results in Figure 8(a) to (d) suggest using the PR ($N\omega = 1$) taper because this taper produced the best curves for predicting MSE using SC . If using the E_a error metric, the results in Figure 8(e) to (h) suggest the PR ($N\omega = 1$) taper because this taper produced the lowest range of E_a values and also the best curves for predicting E_a from SC . If using the E_f error metric, the results in Figure 8(i) to (l) suggest using the PR ($N\omega = 4$) taper because this taper type produced the lowest E_f values and similar curves for predicting E_f based on SC . If it is desired to

estimate both EAC and ESD using tapers with gaps, then a strategy of using two types of tapers to obtain estimates could be employed, that is, using PR ($N_{\omega} = 1$) to obtain the EAC estimate and PR ($N_{\omega} = 4$) to obtain the ESD estimate.

The location of the gap within the taper is also an important factor to consider. For example, the truncation effects associated with some of the non-specially designed tapers (i.e., HnG, SNG) would not be as great for a gap near the taper edge compared with a gap near the taper center. It may be possible that non-specially designed tapers with gaps could be used for gaps near the taper edge and specially designed tapers could be used otherwise. Further study of the effects of tapers with gaps on BSC estimation would be needed to answer this question.

The SAP threshold process for separating diffuse and coherent components is currently the best method of which the authors are aware for performing signal decomposition. It is possible that some nondiffuse scatterers will remain indistinguishable using a simple amplitude criterion. New methods for signal decomposition (e.g., frequency domain approaches) may be developed in the future. Such new methods could be easily incorporated to create the gap locations for generating tapers with gaps.

Conclusion

A method to estimate BSCs using tapers with gaps was presented in this work. The method is applicable when signals from coherent objects are present and the goal is to estimate BSCs based on diffuse scattering. Gaps can be placed at the locations of the signals that are undesirable for the purpose of BSC estimation, allowing for BSC estimation based on diffuse scatterers only. Once BSCs based on diffuse scatterers have been estimated, QUS parameters such as the ESD and EAC can also be estimated based only on diffuse scatterers.

Declaration of Conflicting Interests

The author(s) declared no potential conflicts of interest with respect to the research, authorship, and/or publication of this article.

Funding

The author(s) disclosed receipt of the following financial support for the research, authorship, and/or publication of this article: This work was funded by Grant NIH R01-EB008992.

References

1. Lizzi FL, Greenbaum M, Feleppa EJ, Elbaum M, Coleman DJ. Theoretical framework for spectrum analysis in ultrasonic tissue characterization. *J Acoust Soc Am*. 1983;73:1366-73.
2. Insana MF, Wagner RF, Brown DG, Hall TJ. Describing small-scale structure in random media using pulse-echo ultrasound. *J Acoust Soc Am*. 1990;87:179-92.
3. Insana MF, Hall TJ. Parametric ultrasound imaging from backscatter coefficient measurements: image formation and interpretation. *Ultrason Imaging*. 1990;12:245-67.
4. Feleppa EJ, Lizzi FL, Coleman DJ, Yaremko MM. Diagnostic spectrum analysis in ophthalmology: a physical perspective. *Ultrasound Med Biol*. 1986;12:623-31.
5. Feleppa EJ, Kalisz A, Sokil-Melgar JB, Lizzi FL, Liu T, Rosado AL, et al. Typing of prostate tissue by ultrasonic spectrum analysis. *IEEE Trans Ultrason Ferroelectr Freq Control*. 1996;43:609-19.
6. Lizzi FL, King DL, Rorke MC, Hui J, Ostromogilsky M, Yaremko MM, et al. Comparison of theoretical scattering results and ultrasonic data from clinical liver examinations. *Ultrasound Med Biol*. 1988;14:377-85.
7. Oelze ML, O'Brien WD Jr, Blue JP, Zachary JF. Differentiation and characterization of rat mammary fibroadenomas and 4T1 mouse carcinomas using quantitative ultrasound imaging. *IEEE Trans Med Imaging*. 2004;23:764-71.

8. Mamou J, Coron A, Oelze ML, Saegusa-Beecroft E, Hata M, Lee P, et al. Three-dimensional high-frequency backscatter and envelope quantification of cancerous human lymph nodes. *Ultrasound Med Biol.* 2011;37:345-57.
9. Varghese T, Donohue KD. Mean-scatterer spacing estimates with spectral correlation. *J Acoust Soc Am.* 1994;96:3504-15.
10. Georgiou G, Cohen FS. Tissue characterization using the continuous wavelet transform. Part I: decomposition method. *IEEE Trans Ultrason Ferroelectr Freq Control.* 2001;48:355-63.
11. Insana MF, Wagner RF, Garra BS, Brown G, Shawker TH. Analysis of ultrasound image texture via generalized Rician statistics. *Opt Eng.* 1986;25:743-8.
12. Abeyratne UR, Petropulu AP, Reid JM. On modeling the tissue response from ultrasonic B-scan images. *IEEE Trans Med Imaging.* 1996;4:479-90.
13. Donohue KD, Forsberg F, Piccoli CV, Goldberg BB. Analysis and classification of tissue with scatterer structure templates. *IEEE Trans Ultrason Ferroelectr Freq Control.* 1999;46:300-10.
14. Donohue KD, Huang L, Burks T, Forsberg F, Piccoli CW. Tissue classification with generalized spectrum parameters. *Ultrasound Med Biol.* 2001;27:1505-14.
15. Oelze ML, O'Brien WD Jr. Improved scatterer property estimates from ultrasound backscatter for small gate lengths using a gate-edge correction factor. *J Acoust Soc Am.* 2004;116:3212-23.
16. Luchies AC, Ghoshal G, O'Brien WD Jr, Oelze ML. Quantitative ultrasonic characterization of diffuse scatterers in the presence of structures that produce coherent echoes. *IEEE Trans Ultrason Ferroelectr Freq Control.* 2012;59:893-904.
17. Fodor IK, Stark PB. Multitaper spectrum estimation for time series with gaps. *IEEE Trans Signal Process.* 2000;48:3472-83.
18. Fodor IK. Spectrum estimation in helioseismology. PhD dissertation, Statistics Department, University of California, Berkeley, 1999.
19. Smith-Boughner LT, Constable C. Spectral estimation for geophysical time series with inconvenient gaps. *Geophys J Int.* 2012;190:1404-22.
20. Chen X, Phillips D, Schwarz KQ, Mottley JG, Parker KJ. The measurement of backscatter coefficient from a broadband pulse-echo system: a new formulation. *IEEE Trans Ultrason Ferroelectr Freq Control.* 1997;44:515-25.
21. Lavarello R, Ghoshal G, Oelze ML. On the estimation of backscatter coefficients using single-element focused transducers. *J Acoust Soc Am.* 2011;129:2903-11.
22. Oelze ML, O'Brien WD Jr, Blue JP, Zachary JF. Differentiation and characterization of rat mammary fibroadenomas and 4T1 mouse carcinomas using quantitative ultrasound imaging. *IEEE Trans Med Imaging.* 2004;23:764-71.
23. Vogt M, Opretzka J, Ermert H. Parametric imaging of specular reflections and diffuse scattering of tissue from multi-directional ultrasound echo signal data. In: *Proceedings of the IEEE Ultrasonics Symposium, Beijing, China, 2-5 November 2008*, pp. 1963-6.
24. Cohen FS, Georgiou G, Halpern E. WOLD decomposition of the backscatter echo in ultrasound images of soft tissue organs. *IEEE Trans Ultrason Ferroelectr Freq Control.* 1997;44:460-72.
25. Georgiou G, Cohen FS. Tissue characterization using the continuous wavelet transform. Part II: application on breast RF data. *IEEE Trans Ultrason Ferroelectr Freq Control.* 2001;48:364-73.
26. Daubechies I. The wavelet transform time-frequency localization and signal analysis. *IEEE Trans Inf Theory.* 1990;36:961-1004.
27. Torrence C, Compo GP. A practical guide to wavelet analysis. *Bull Am Meteorol Soc.* 1998;79:61-78.
28. Percival DB, Walden AT. *Spectral Analysis for Physical Applications: Multitaper and Conventional Univariate Techniques.* Cambridge, UK: Cambridge University Press; 1993.
29. Riedel KS, Sidorenko A. Minimum bias multiple taper spectral estimation. *IEEE Trans Signal Process.* 1995;43:188-95.
30. Wear KA, Stiles TA, Frank GR, Madsen EL, Cheng F, Feleppa EJ, et al. Interlaboratory comparison of ultrasonic backscatter coefficient measurements from 2 to 9 MHz. *Ultrasound Med Biol.* 2005;24:1235-50.